TEKTONIKA

Supporting Information (SI)

for

From a Continental Margin to an Alpine Dome: 4D Geodynamic Evolution of the Aar Massif

Ferdinando Musso Piantelli[1,2*], Lukas Nibourel[3], Alfons Berger[2], and Marco Herwegh[2]

[1] Federal Office of Topography swisstopo, Seftigenstrasse 264, 3084 Bern, Switzerland
[2] Institute of Geological Sciences, University of Bern, Baltzerstrasse 1+3, 3012 Bern, Switzerland
[3] ETH Zürich, Department of Earth Sciences, Sonneggstrasse 5, 8092 Zürich, Switzerland

[*] Corresponding author: ferdinando.musso@unibe.ch

Content

1. GEOLOGICAL PROFILE AND FIELD VIEWPOINT COORDINATES

Profile		X	Y
A-A’	A	2604690	1152818
	A’	2627340	1118096
B-B’	B	2626079	1166814
	B’	2647107	1134196
C-C’	C	2644283	1178708
	C’	2662489	1147231
D-D’	D	2666273	1192525
	D’	2682556	1161768
E-E’	E	2690006	1203758
	E’	2704486	1170118
F-F’	F	2709533	1211747
	F’	2723412	1179849
α-α’	α	2604690	1152818
	α’	2700115	1093525
Viewpoint 1	VieP.1	2634550	1150655
Viewpoint 2	VieP.2	2713679	1185797
Viewpoint 3	VieP.3	2676067	1173782
Field location c		2643327	1139477
Field location d		2653815	1152306
Field location e		2632115	1144810

Table S1. Table containing the coordinates of the investigated profiles and of the viewpoints of the field locations described in the article. Coordinate system: CH1903+ /LV95.

2. 2D DATASET COMPILATION

The 2D dataset used for this study was compiled from a wide range of data published by swisstopo (until 2022) or in scientific publications. This dataset consists of:

Maps The initial dataset was compiled from the following pre-existing maps: Krebs (1925), Collet and Paréjas (1928), Mair et al. (2018), and the GeoCover vector datasets (swisstopo) containing the following mapsheets: LK no. 1191, 1192, 1193, 1210, 1211, 1212, 1213, 1229, 1230, 1231, 1232, 1233, 1248, 1249, 1250, 1251, 1252, 1267, 1268, 1269, 1270, 1287, 1288, and 1289. In addition, the Geological Special Map 1:100’000 of the Aar Massif, Tavetsch, and Gotthard Nappes of the Swiss Geological Survey (Berger et al., 2017) was used to understand the geological architecture at the regional scale and to define the lithostratigraphic and structural project legend.

Geological profiles All the available profiles of the Geological Atlas of Switzerland; published profiles of: Pfiffner et al. 2011; Nibourel et al. 2021; Hänni and Pfiffner, 2001; Herwegh and Pfiffner, 2005; Krayenbuhl and Steck, 2009 and Mair et al., 2018.

Seismic data Seismic profiles published in Diehl et al., 2021; Pfiffner et al., 1997, NEAT 9001 and lines W1, C1 and E1.

Orthophoto SwissImage with a raster resolution of 0.25 x 0.25 m; provided by swisstopo

DEM Swiss ALTI3D with a downsampled raster resolution of 2 x 2 m, version 2013 provided by swisstopo

Hillshade maps Derived from the DEM and generated in ArcGIS (ESRI’s ArcGIS, v.10.8).

Structural work The structural work compiled from the PhD theses of Baumberger, 2015; Wehrens, 2015; Nibourel 2019 and Musso Piantelli 2023.

2.1. Data validation, interpretation below Quaternary cover and fieldwork

Due to discrepancies between the individual map sheets, or scientific publications, the entire dataset underwent a validation and homogenisation process to produce a geologically consistent bedrock map of the Aar Massif (Fig. S1). The process was carried out in in ArcGIS (ESRI's ArcGIS, v.10.8) working at the scale of 1:25'000. Lithological and structural boundaries were verified and updated remotely using the high-resolution orthophotos and digital elevation model (DEM). In the case of Quaternary cover (e.g., moraine deposits, glaciers), the underlying trends of stratigraphic and tectonic boundaries were interpreted.

To extend the structural dataset, a fault zone map (1:25'000) was generated on remotely sensed images following the workflow of Baumberger et al. (2022), see also Musso Piantelli et al. (2023). On the basis of the kinematics of the structures described in previous studies and field information the structural sets were subdivided as indicated in Chapter 4. Data were verified in the field at key locations by mapping and collecting structural field data (see Musso Piantelli et al., 2022 and 2023). The kinematics of the structures were characterised by the compilation of over 2'500 field measurements (fault planes dip direction/dip angle, and stretching lineations; of which over 1000 collected in this study), and by the generation of rose-plots automatically derived from the striking of the remotely-detected structures (Fig. A2).

2.2 The Aar Massif 3D Project Map

The result of the compilation and validation process was the generation of the project bedrock map of the massif. The map includes all the lithological units and structural elements, which were then used as the 2D input dataset for the construction of the 3D geological model. For the purposes of this publication, the map shown in Fig. S1 was simplified to the map shown in Fig. 1. In this simplification: (i) the sedimentary cover of the massif was summarised as 'par/autochtonous cover'; (ii) the intrusions were grouped into a single group named 'Variscan and post-Variscan intrusions'; (iii) the different groups of pre-Variscan basement were grouped into the generic term 'basement units'.

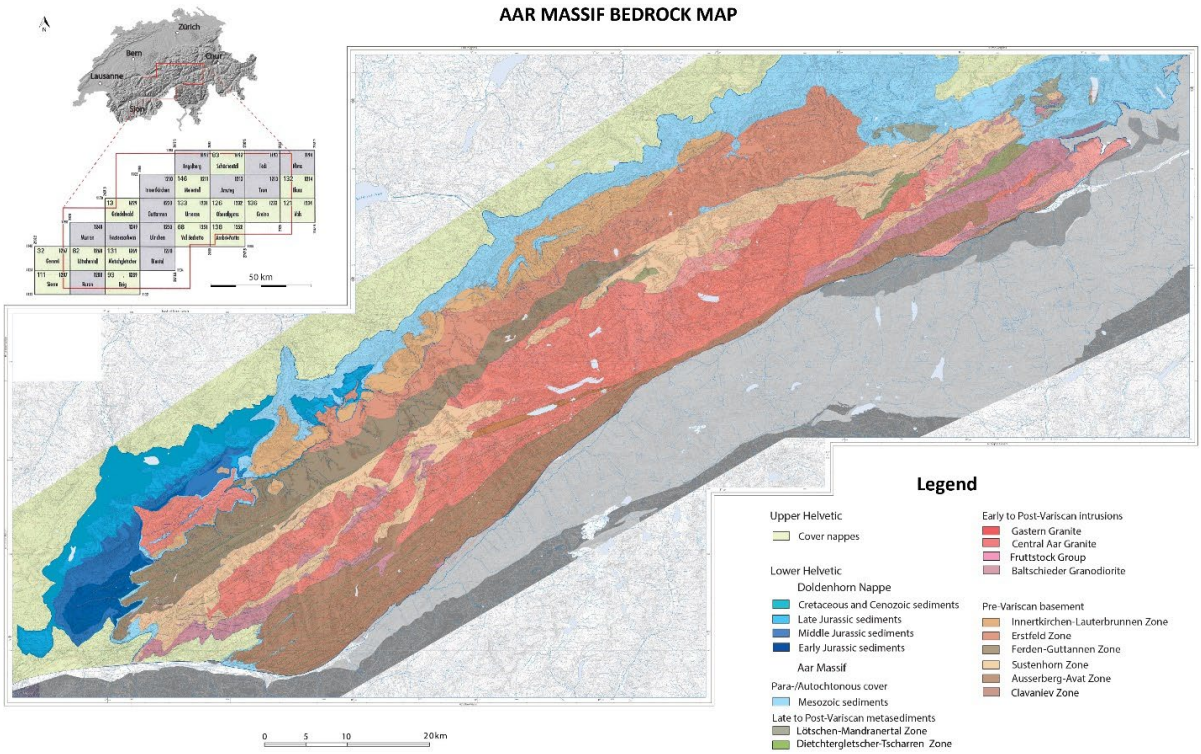

Figure S1. The result of the compilation and validation of the 2D dataset was the generation of the bedrock map of the Aar Massif. The map includes all the lithological units and structural elements, which were then used as input for the construction of the 3D geological model.

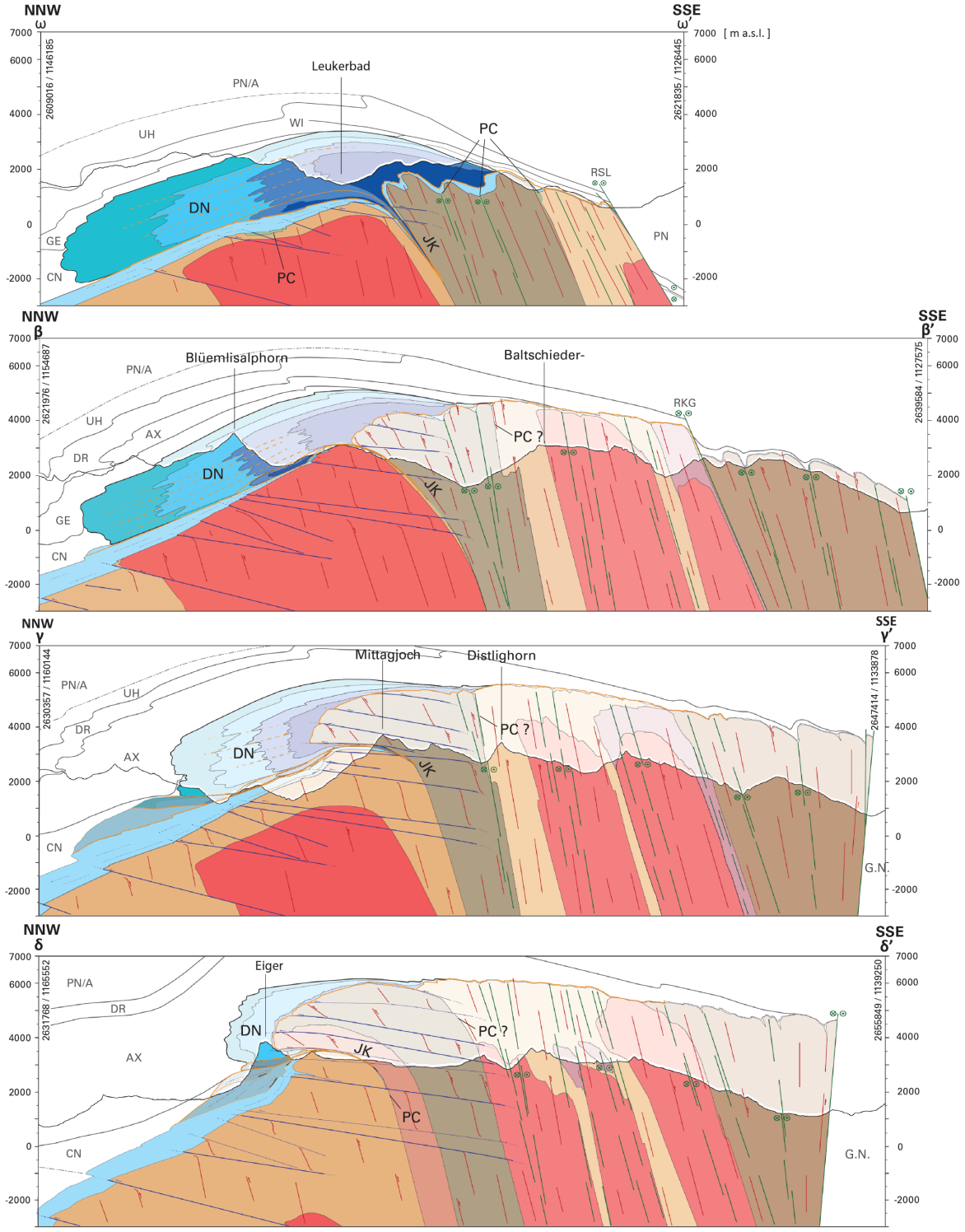

Figure S2. Reference geological cross-sections through the western side of the massif. The profiles are modified after Musso Piantelli et al. 2022. Overlying nappes: GE, Gellihorn; WI: Wildhorn; AX: Axen; DR: Drusberg; UH: Ultrahelvetic; CN: Cenozoic sediments; PN/A: Penninic and Austroalpine sediments. In sections ω-ω' and β-β' the outline of the overlying upper Helvetic nappes was modified after Herwegh and Pfiffner (2005) and Hänni and Pfiffner (2001), respectively.

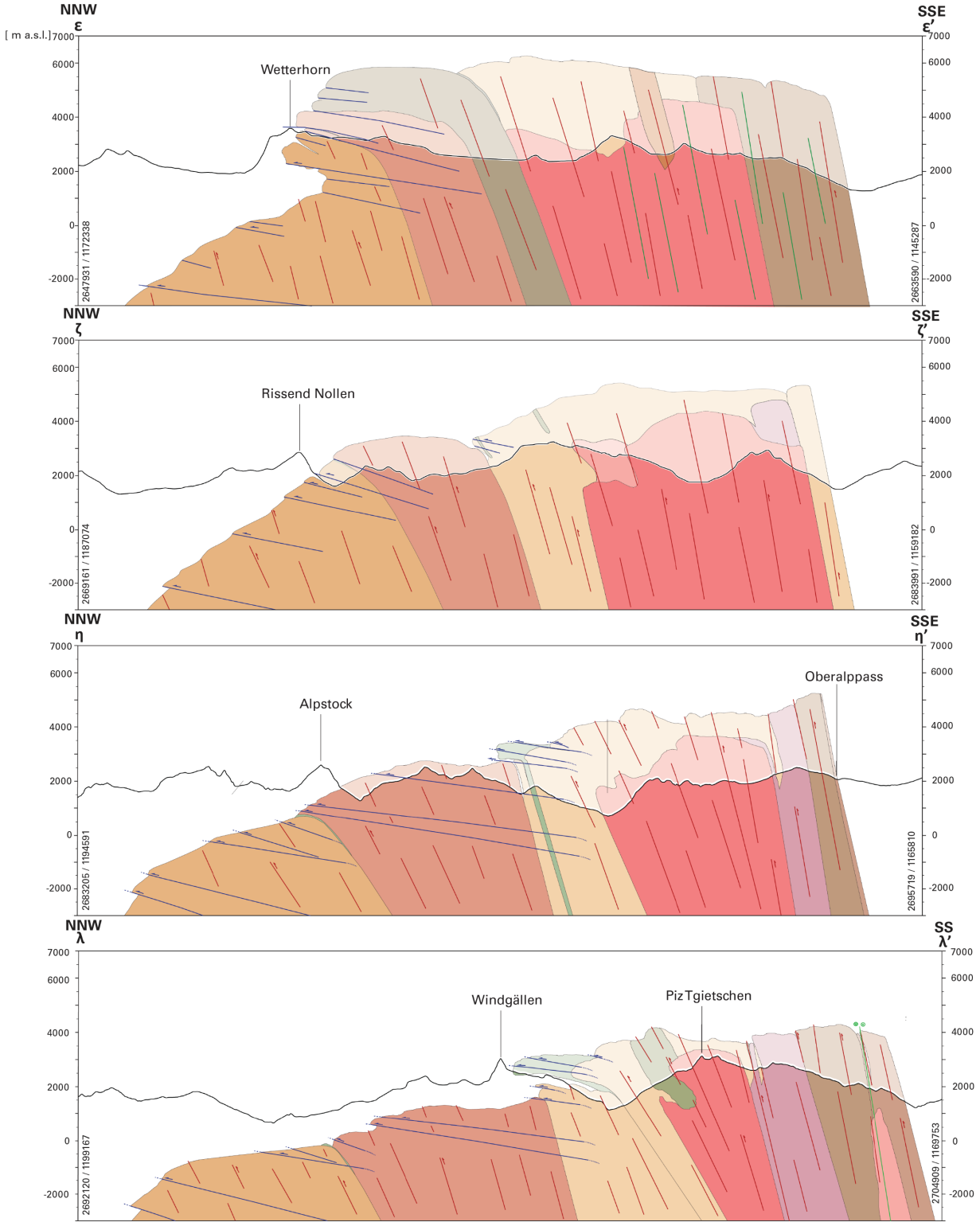

Figure S3. Reference geological cross-sections through the central region of the massif. Profile λ was modified after Nibourel et al., 2021.

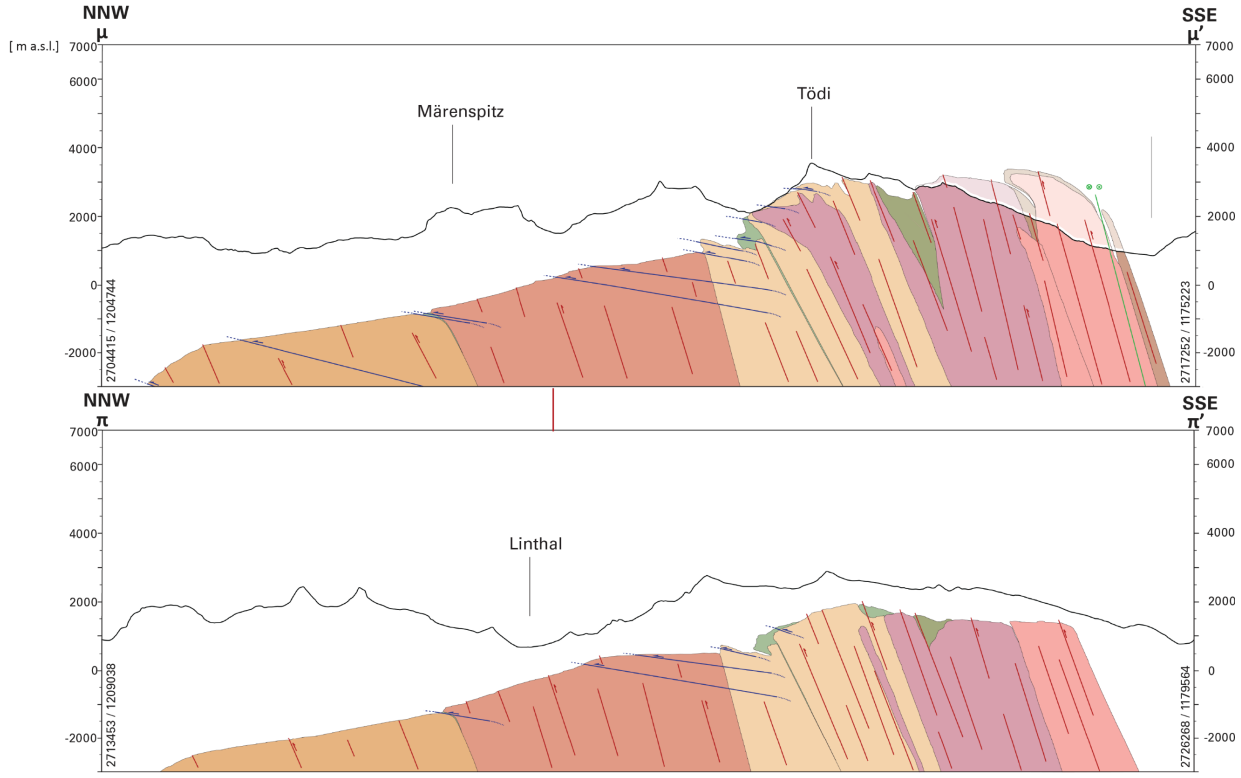

Figure S4. Reference geological cross-sections through the eastern side of the massif.

3. REFERENCE GEOLOGICAL CROSS-SECTIONS

To develop a structurally consistent interpretation of the massif's underground, ten reference geological cross-sections have been constructed along the strike of the massif, perpendicular to the strike of the large-scale structures and boundaries (ω – ω'; to π - π' in the area; see Figs. S2-4). For the construction of the geological cross-sections, surface and contacts line intersections were collected in the software Move™ (Petex, v.2019.1; Fig. S5). Dip-data information, lithological and tectonic boundaries as well as literature data in the vicinity (2000 m) of the cross sections, were orthogonally projected onto the latter to better constrain the geometric and structural relationships of the different units (e.g., Fig. S5). The resulting profiles were used as guideline for the generation of the constructional cross section during the 3D modelling phase.

4. 3D EXPLICIT GEOLOGICAL MODELLING

The produced 2D dataset (bedrock map, lithological and tectonic boundaries, and strike/dip data) was vertically projected onto the high-resolution digital elevation model (DEM) and then loaded into the software Move™ (Petex, v.2019.1). Given the complex geometries of the geological units, we adopted an *explicit modelling approach* to construct the 3D geological model. We are aware that an *implicit 3D modelling approach* would have been generally preferable, as more mathematically driven, less subjective, and more reproducible than the explicit approach (although even this approach require a considerable number of user-defined rules, which introduces subjectivity similar to that in explicit models). In fact, for this project different implicit modelling software were tested during our workflow to generate the surfaces. However, the large size of our model (surface area ~5'300 km^2), the number of geological units (22), and the highly complex structural setting exceeded the computational capabilities of the implicit software we evaluated. As a result, the generated surfaces lacked the spatial resolution needed to address

the project's central scientific questions. For these reasons, we adopted an explicit modelling strategy, implemented in two main phases:

a) Constructional cross section generation

Throughout the area and based on the structural concepts developed with the reference geological profiles, a multiple set of over 330 constructional geological cross sections was generated with a regular spacing of 500 m Fig. S6a). With an alternation of projection techniques, and mesh generation along each constructional cross-section, the geological boundaries and structures were developed with lines in an along length sampling interval of 25 m (Fig. S6a).

b) 3D Interpolation

All digitized lines for each modelling horizon of the constructional cross sections were combined with continuous 3D spatial information derived from: (i) lithostratigraphic and structural contacts of model units exposed between ~400 m and ~4200 m a.s.l. (yellow line in Fig. S5a); (ii) borehole and railway tunnel logs from the Lötschberg–Gotthard transect; and (iii) all available seismic data. Using these datasets, 3D interpolation was carried out with a spline curve meshing technique to generate a triangulated surface (mesh) for each modelling horizon (Fig. S6b). The resulting 3D geological model comprises a series of meshes representing the top surfaces of major lithological units and tectonic boundaries. The model extends from the interpreted surface topography down to −3 km a.s.l., except along the northern front of the massif, where it reaches −6 km a.s.l. to capture the frontal thrust. Each mesh has a 50 m grid size and follows the principle of a watertight (sealed) model. Accordingly, every stratigraphic horizon is defined continuously across the area of interest, intersecting cleanly with lateral boundaries, faults, unconformities, or erosion surfaces (e.g., Caumon et al., 2004).

4.1 Uncertainties estimation

The maximum resolution of the model is defined by the 1.25'000 scale at which the 2D input dataset was sorted at the surface. Moving away from the surface and the underground tunnel data the resolution varies within the model. However, within 400 and 4200 m a.s.l., representing the highest and lowest topographic points of the area, the model fits the input data with an uncertainty of ±200m (see Musso Piantelli et al., 2023). The interpretation above topography of the basement/sediment contact was constrained by the 3D shape of the contact on the western, eastern sides and the northern front of the massif. Below 400 m a.s.l., the profiles have been drawn with at the scale of 1:25'000, however uncertainties deriving from (i) data source; (ii) interpretation, and (iii) lack of data, were not estimated.

Research into the development of methods for quantifying uncertainty in models has made progress in recent years (Bond et al., 2011; Wellmann and Regenauer-Lieb, 2012; Wellmann et al., 2014; Schneeberger et al., 2017; Wellmann and Caumon, 2018; Pakyuz-

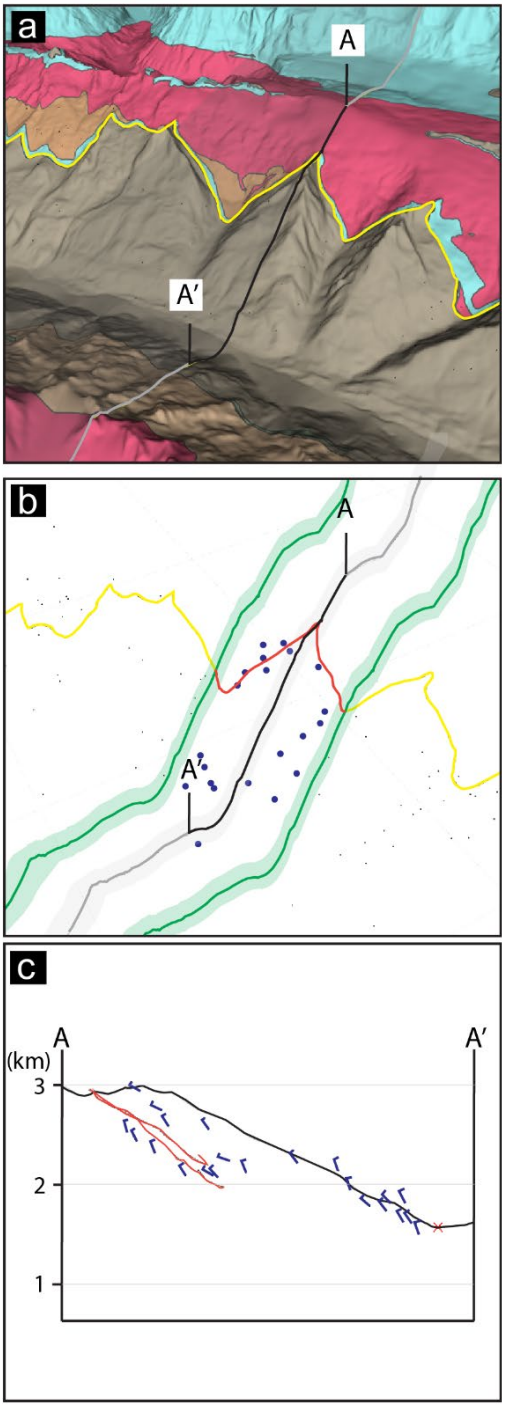

Figure S5. (a) Data are projected onto the DEM and imported in MoveTM. (b) All the data lying within 2 km on either side of the cross section are selected. (c) The data are normally projected onto the cross section. Red line: sediment/basement contact; blue symbols: dip/strike indications; x point: intersection with fault plane.

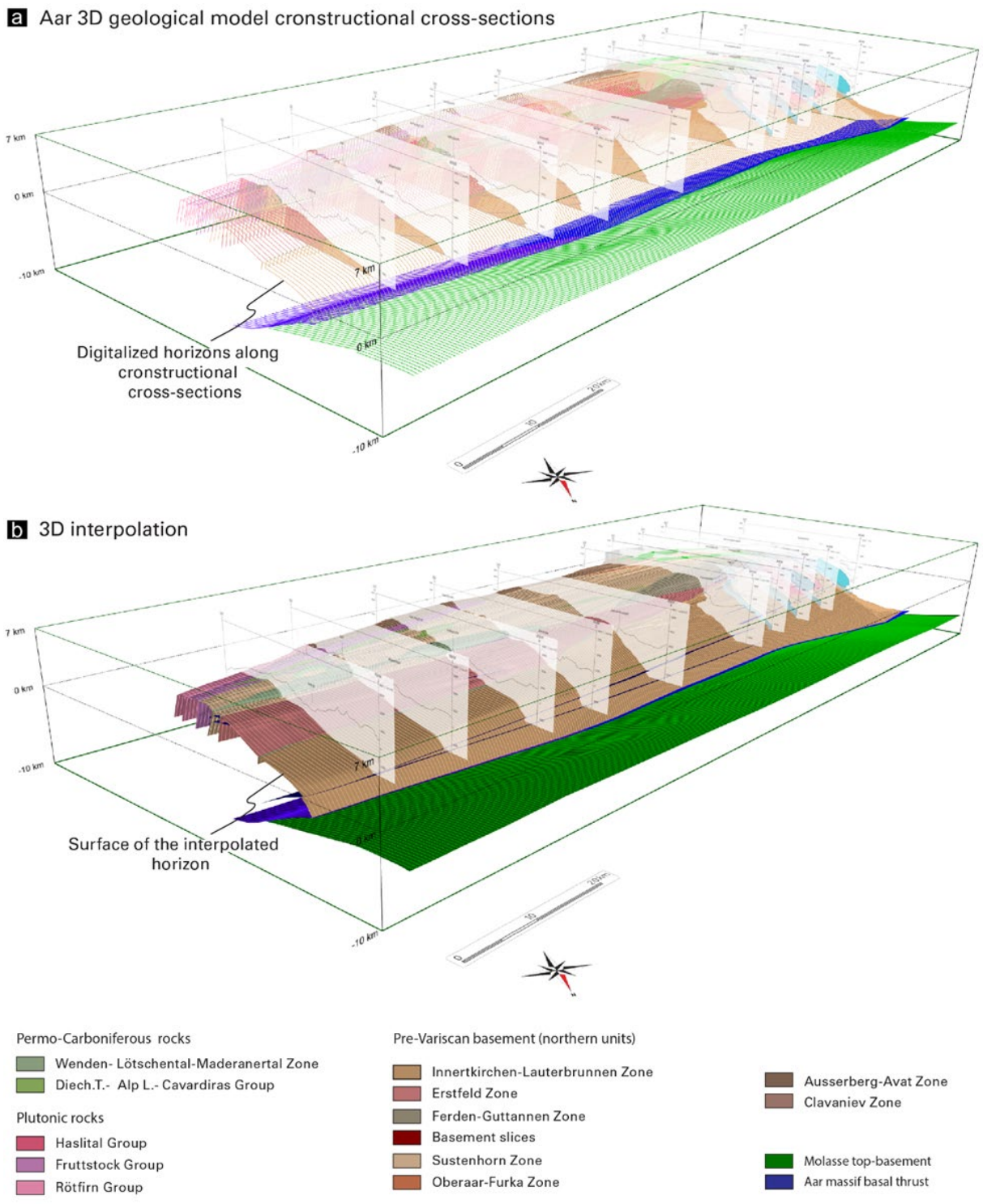

Figure S6. 3D block diagrams that show the modelling sequence followed for constructing the 3D geological model of the massif. (A) Generation of regularly 500 m spaced constructional cross-sections and line digitalization of the modelled horizons along the sections. (B) 3D interpolation: by applying 3D projection and meshing techniques, surface and cross-sections boundaries are interpolated generating surfaces for each horizon of the model.

Charrier et al., 2018; Baumberger et al., 2022). However, most of the contributions focus on simplified geological settings (e.g., Wellmann et al., 2010) and very few studies concern Alpine domains (e.g., Brisson et al., 2023). Methodologies for assessing uncertainties in 3D models of complex geological settings are not yet fully developed. For this reason, no further uncertainty quantification was carried out within the framework of this project.

5. CROSS SECTION RESTORATION

The six cross sections presented in the manuscript (AA' to FF') were retro-deformed by performing line-balancing (i.e., for the crystalline basement – sedimentary cover contact, Fig. S7). During restoration, no material displacement outside the cross-section planes was assumed. As the sections strike parallel to the Alpine stretching lineations, area conservation during Alpine shortening (i.e., reverse faulting and thrusting; NNW-SSE) appears to be a robust assumption. The only exception concerned the strike-slip deformation phase of the basement units (Oberaar, Wehrens et al. 2016, 2017). The strike-slip displacement was partitioned into a large number of shear zones and it is difficult to quantify in the field. However, at the contact between the sedimentary cover and the basement in the western Aar Massif, the displacement is limited to a few meters at maximum, indicating small displacement only. For this reason, the strike-slip phase was neglected as a first order of approximation and therefore not included into the overall estimation of shortening and exhumation of the basement units.

The Triassic layers of the autochthonous sedimentary cover were used as proxies to characterize the basement top shape and to quantify basement shortening (l1 and l2 Fig. S7). The top basement was restored assuming a precollisional geometry of the proximal part of the European passive continental margin, being bent by ~10° underneath the tectonically active boundary of the overriding plate (see Nibourel et al. 2018 and 2021). Herein, the location of Permo-Carboniferous zones and sediment wedges (e.g., Fig. S7) served as a marker allowing us to reconstruct the locations of syn-rift faults utilized during the aperture of the as Doldenhorn, Susten-Windgällen, and Tödi (see Fig. 9). The throws of the bounding normal faults of the basins were reconstructed using the vertical extent of the multiple sedimentary wedges and Permo-Carboniferous troughs as a minimum estimate (e.g., Musso Piantelli et al., 2022).

In the following paragraph, we present the results of the retrodeformation of sections A-A', B-B', C-C', E-E', and F-F' (Figs. S8 to S12) as evolutionary steps, starting from the initiation of Alpine deformation (22 Ma) to the present-day configuration. For the description of the deformation and emplacement of the Aar Massif, see the Results and Discussion chapters (4 and 5).

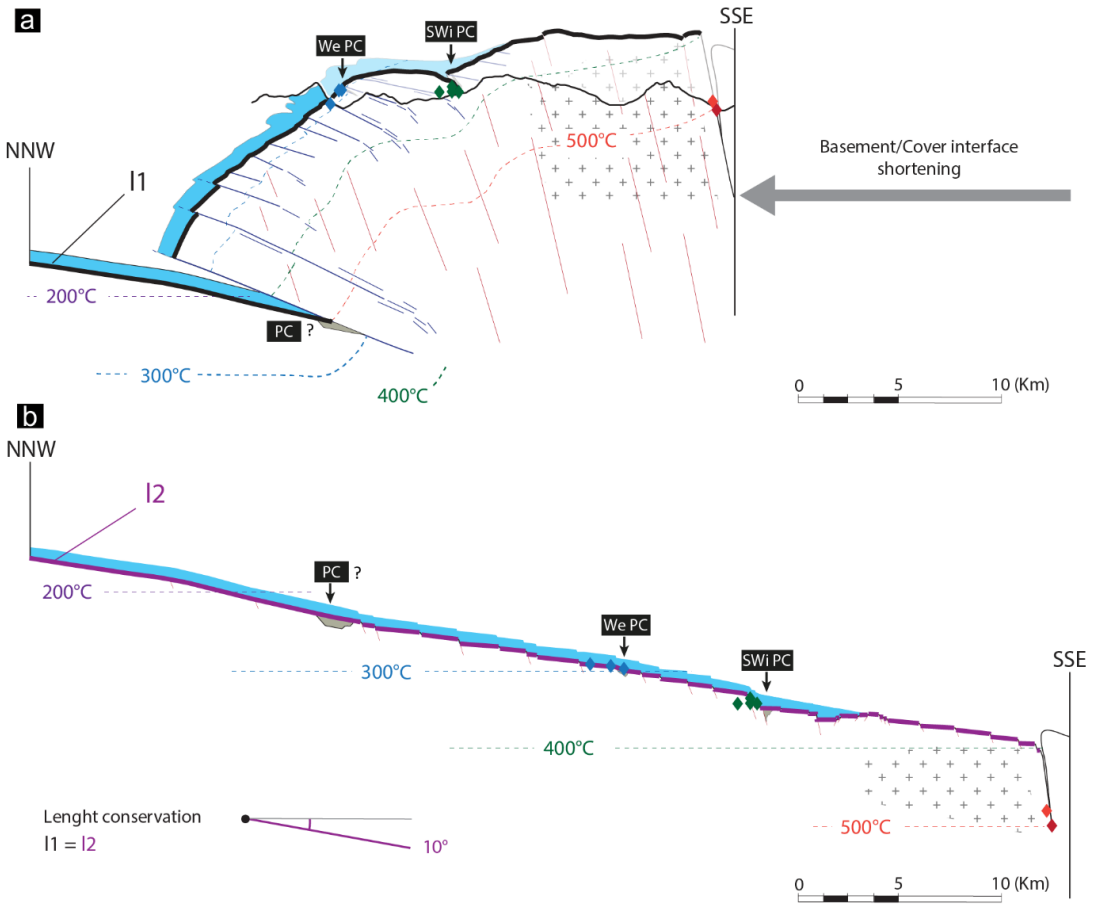

Figure S7 – Cross-section restoration of the Aar Massif. The restoration was performed assuming the conservation of the sedimentary cover/basement interface length (l). (A) Cross-section of the current structural disposition of the Aar Massif basement units, sedimentary cover and Peak temperature data. (B) Restored cross-section.

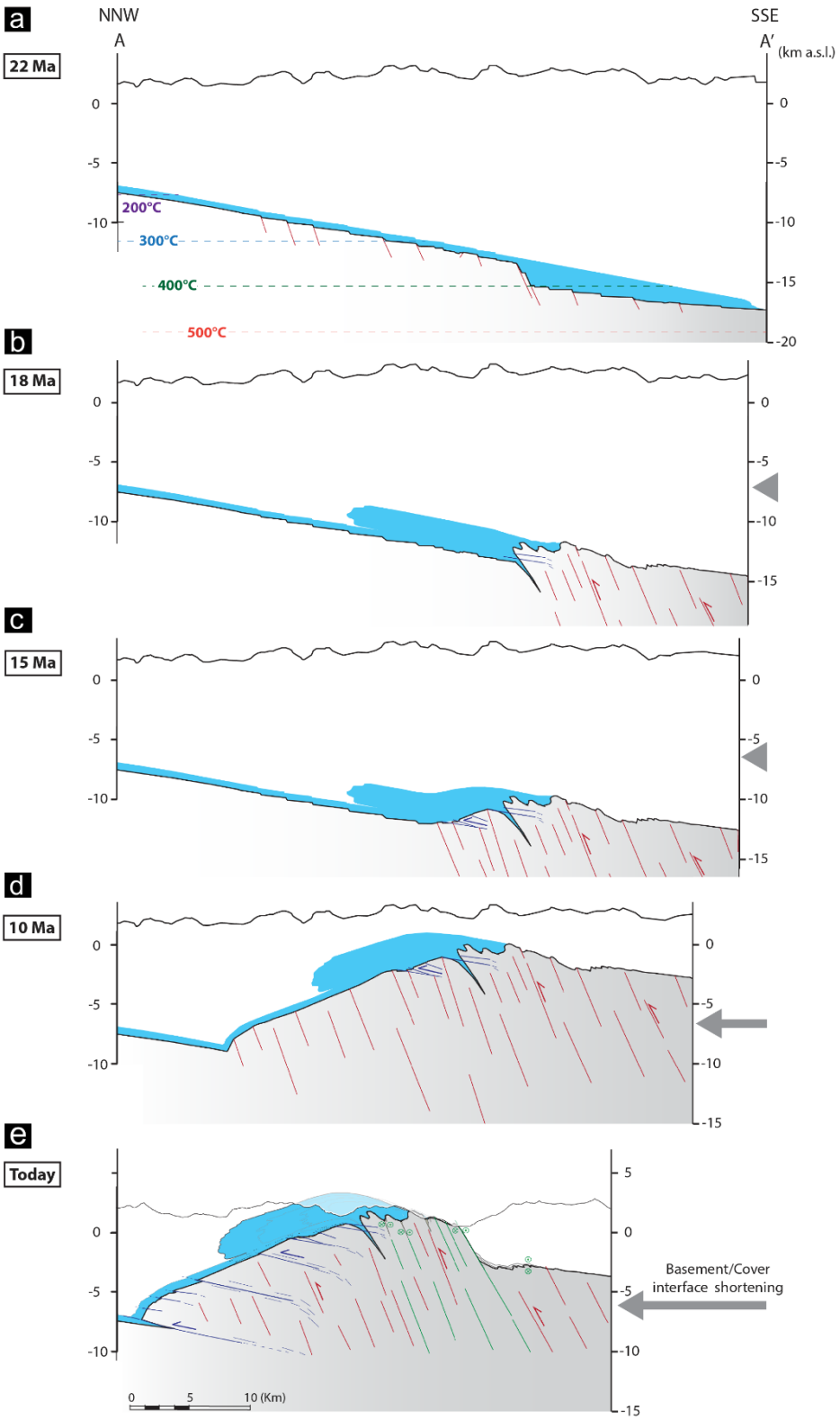

Figure S8. Cross-section restoration of the AA' section from 22 Ma to today.

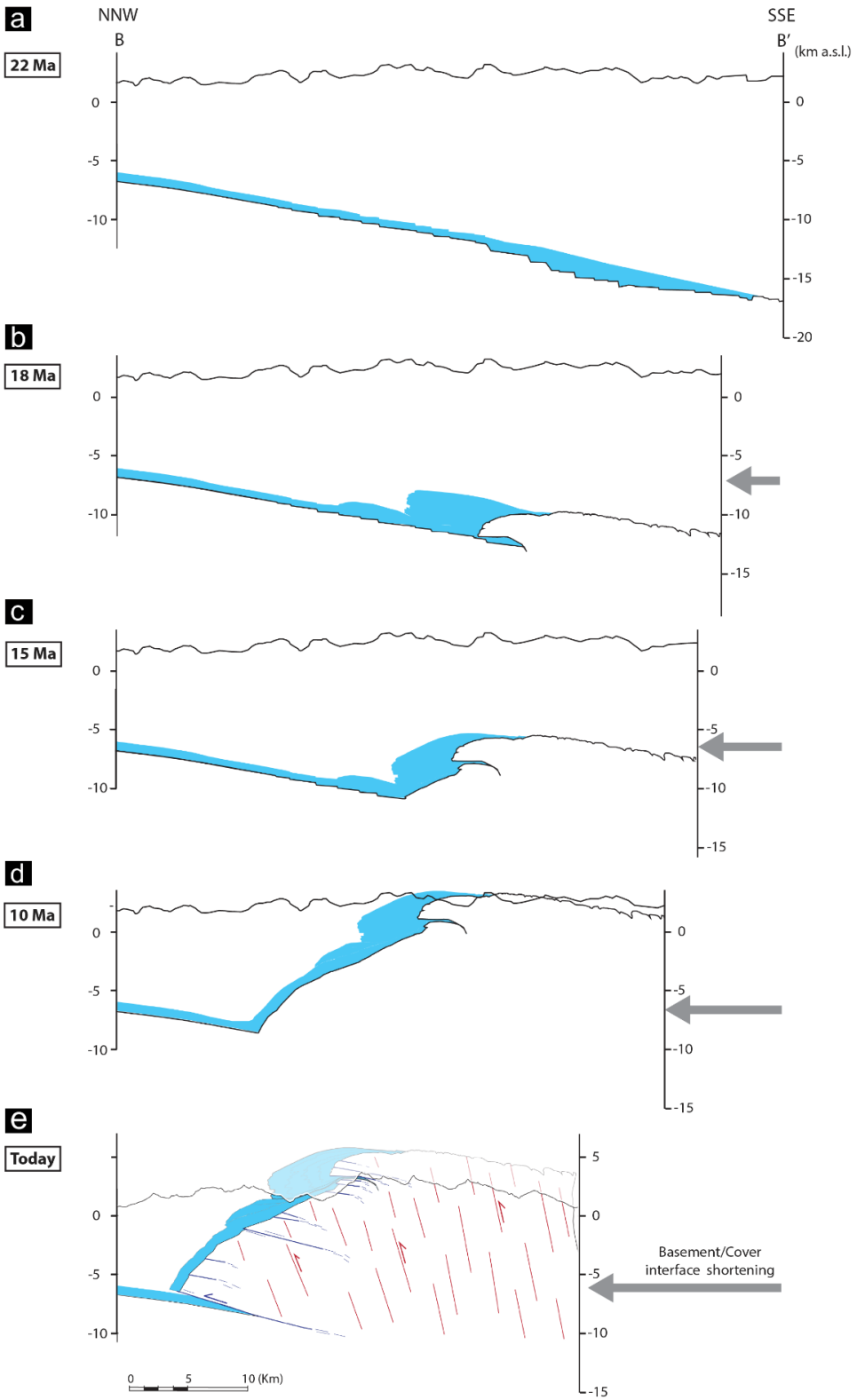

Figure S9. Cross-section restoration of the BB' section from 22 Ma to today.

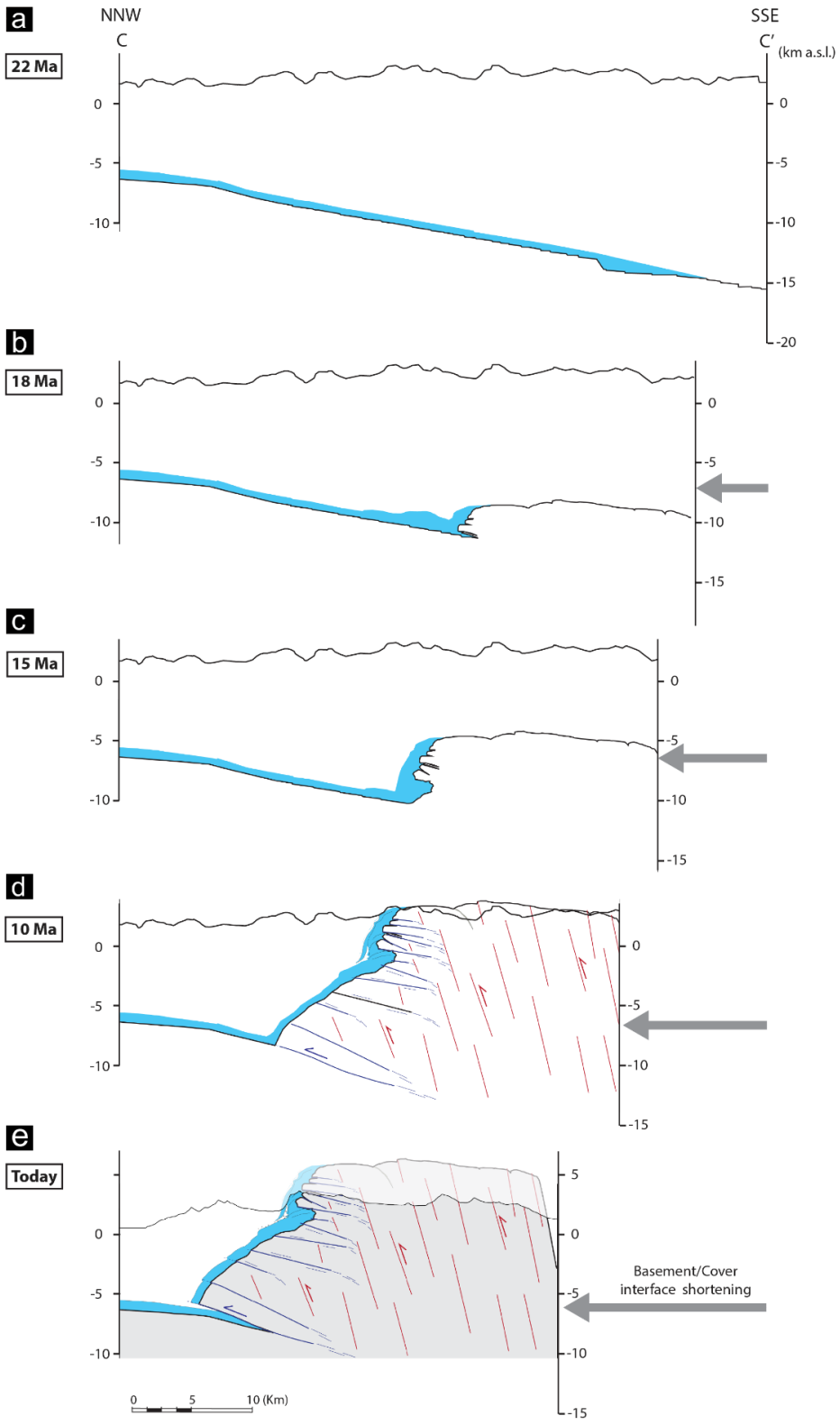

Figure S10. Cross-section restoration of the CC' section from 22 Ma to today.

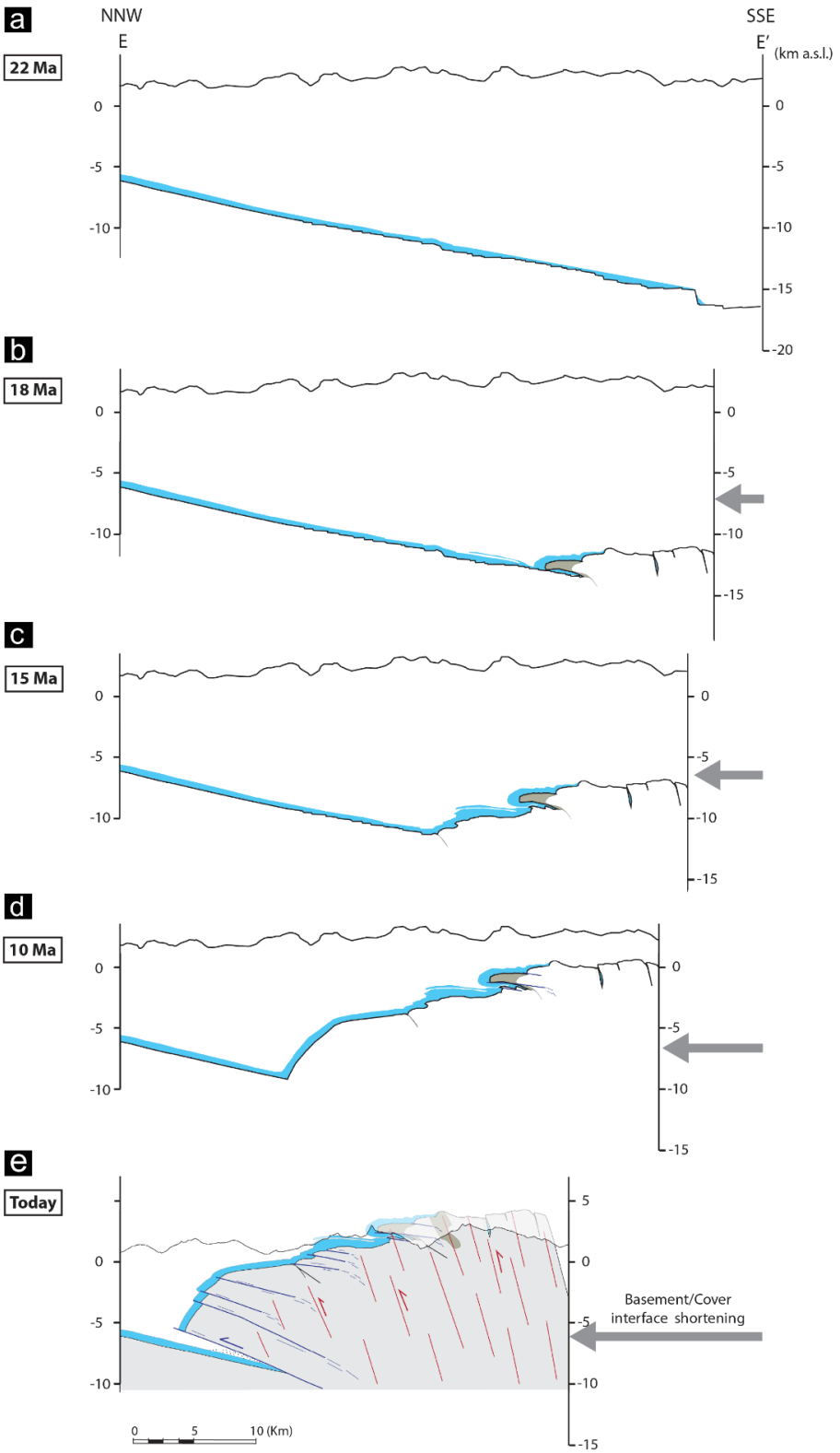

Figure S11. Cross-section restoration of the EE' section from 22 Ma to today.

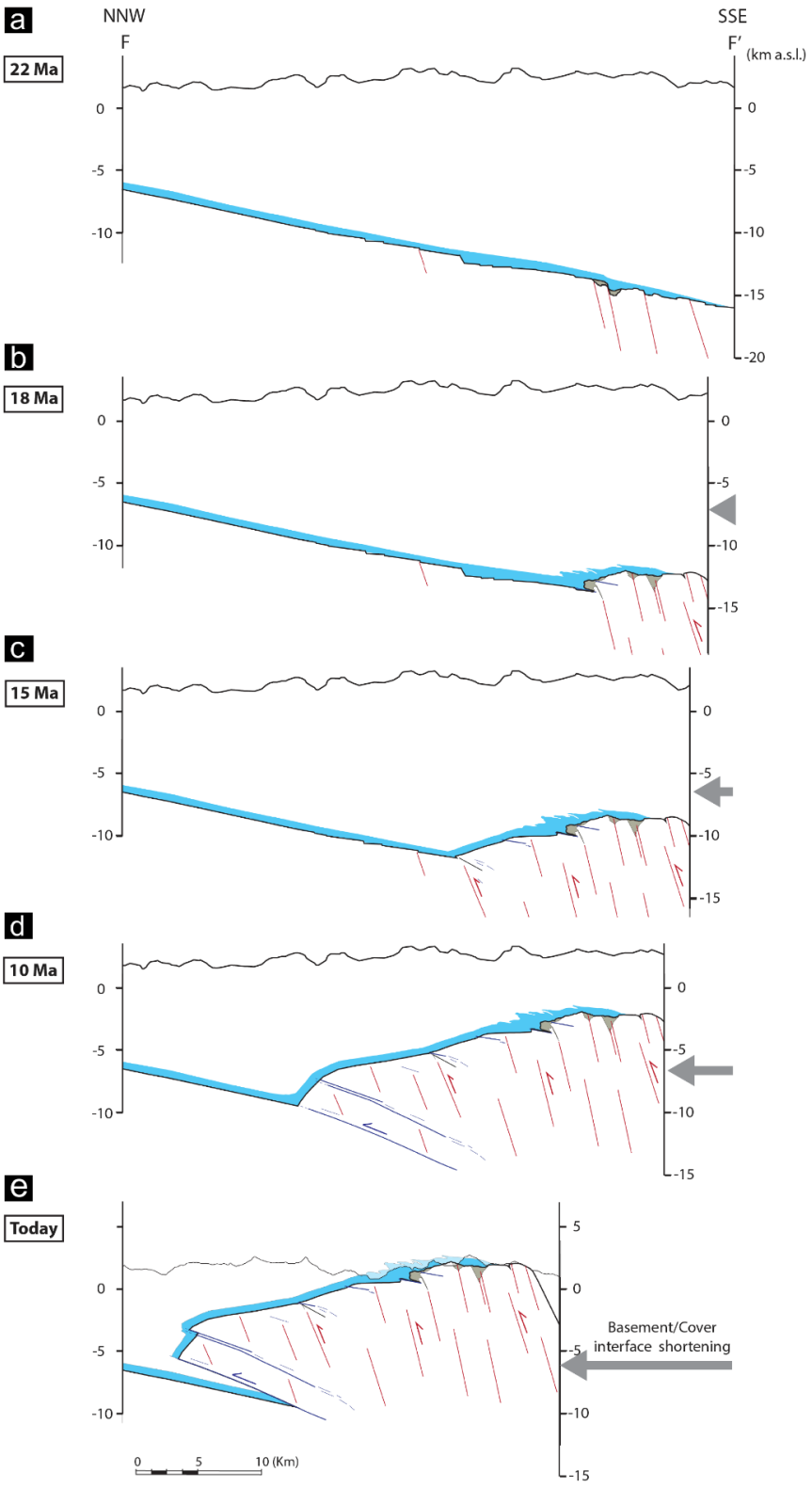

Figure S12. Cross-section restoration of the FF' section from 22 Ma to today.

6. PALEOGRADIENT RECONSTRUCTION

The compilation of peak temperature data of Nibourel et al. 2021 (see references therein) was selected for this study to strengthen our cross-section restoration and 4D reconstruction. Each data point located within 4 km on either side of the six cross sections (AA' to FF'; Fig. 2) and in close proximity to the sedimentary-basement contact, was selected and incorporated into our reconstruction. This results in a dataset of 50 peak temperature datapoints, displayed in Table S2 (see additional information and references therein).

These datapoints were normally projected onto the respective profiles. During the subsequent retrodeformation, the datapoints were also retrodeformed to 22 Ma (Fig. S7). We have therefore reconstructed the position of the T_{max} datapoint at 22 Ma. The resulting reconstruction is shown in map view in Figure S13a, where the upper basement and T_{max} points are located. Consequently, along each profile, where possible, the 300, 350, 400 and 500°C points have been extrapolated or calculated along the shortest connecting lines between the data points. The 300, 350, 400 and 500°C points, with a relative uncertainty of ±50°C, were then normally projected SW-NE along the TT' profile Fig. S13b. Along the resulting profile the gradient of 26°C/km was calculated as the best fitting gradient.

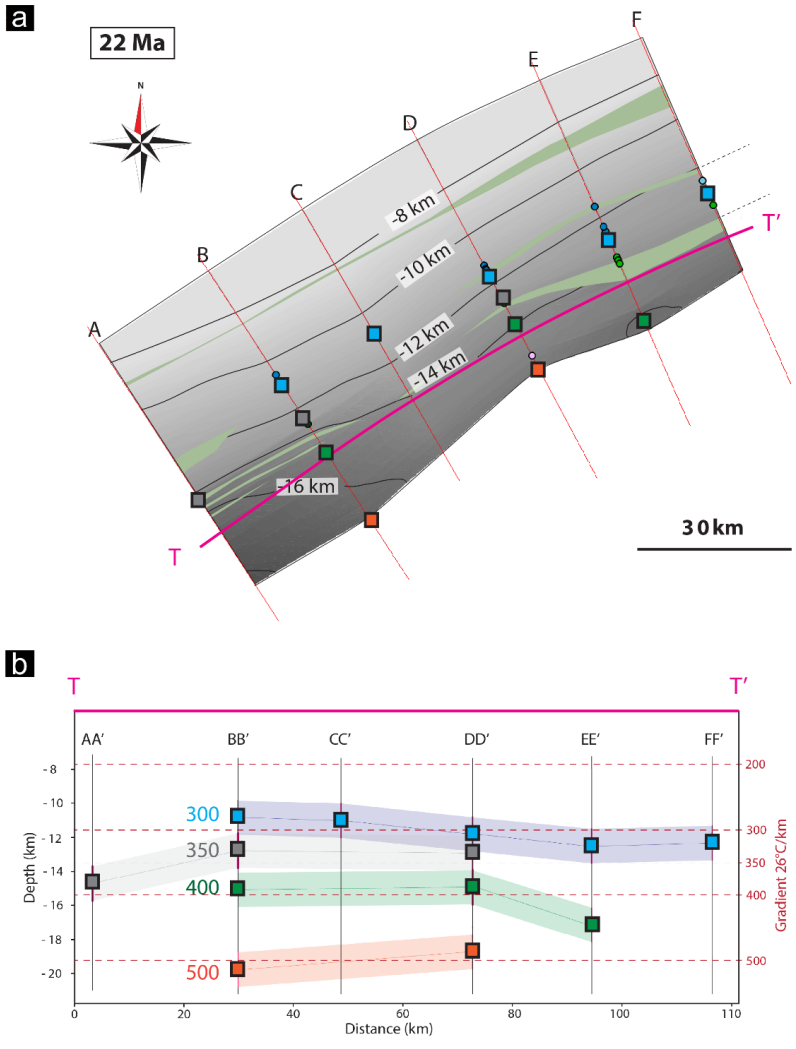

Figure S13 – (A) Map view of the part of the top crystalline units of the passive margin at 22 Ma, from which the Aar Massif developed. The points lying on the cross-section traces correspond to the location of the T_{max} data retrodeformed with the cross sections. (B) Cross-section TT' where the T_{max} data have been normally projected and interpolated with a 26°C/km horizontal geothermal gradient.

Sample name	X	Y	Z	Temperature	2sigma	N	Error	Method	RSCM fitting procedure	Stratigraphic unit	Locality	Reference	Profile
CH1574	2618124	1130872	1385	354	19	na	50	RSCM	Beyssac et al. (2002)	Aar Massif: Upper Jurassic	Doldenhorn nappe	Girault et al. (2021)	AA'
CH1576	2615429	1130976	1320	353	18	na	50	RSCM	Beyssac et al. (2002)	Aar Massif: Upper Jurassic	Doldenhorn nappe	Girault et al. (2021)	AA'
CH1578	2614963	1132531	1310	349	18	na	50	RSCM	Beyssac et al. (2002)	Aar Massif: Lower Jurassic	Doldenhorn nappe	Girault et al. (2021)	AA'
CH1580	2614423	1132863	1375	349	18	na	50	RSCM	Beyssac et al. (2002)	Aar Massif: Lower Jurassic	Doldenhorn nappe	Girault et al. (2021)	AA'
CH1582	2614268	1133530	1450	346	18	na	50	RSCM	Beyssac et al. (2002)	Aar Massif: Lower Jurassic	Doldenhorn nappe	Girault et al. (2021)	AA'
CH1583	2614036	1133863	1490	353	19	na	50	RSCM	Beyssac et al. (2002)	Aar Massif: Lower Jurassic	Doldenhorn nappe	Girault et al. (2021)	AA'
CH1585	2614729	1133864	1635	345	18	na	50	RSCM	Beyssac et al. (2002)	Aar Massif: Lower Jurassic	Doldenhorn nappe	Girault et al. (2021)	AA'
CH1588	2613650	1134306	1305	349	18	na	50	RSCM	Beyssac et al. (2002)	Aar Massif: Lower Jurassic	Doldenhorn nappe	Girault et al. (2021)	AA'
BT3–BT5	2619624	1143808	780	347	na	307	na	dC Eqn. 2	na	Aar Massif: Carboniferous	Loetschberg base tunnel	Berger et al. (2020), Williams (2008)	AA'
BT6	2618720	1145060	780	357	na	316	na	dC Eqn. 2	na	Aar Massif: Carboniferous	Loetschberg base tunnel	Berger et al. (2020), Williams (2008)	AA'
Lau-02	2636387	1157680	838	283	11	24	40	RSCM	Luensdorf (2017) poly3	Aar Massif: Upper Jurassic (carbonate dominated)	Lauterbrunnen Truemmelbachfaelle	Mair2018	BB'
Si1325	2645820	1131020	1160	518	11	18	50	RSCM	Beyssac et al. (2002)	Penninic or Austroalpine	Gt	Hafner (2014)	BB'
Si1327	2644010	1131360	690	497	48	24	50	RSCM	Beyssac et al. (2002)	Penninic or Austroalpine	Gt	Hafner (2014)	BB'
Si1329	2646650	1133260	980	497	27	21	50	RSCM	Beyssac et al. (2002)	Penninic or Austroalpine	Gt	Hafner (2014)	BB'
GS-126	2632350	1150050	2325	361	na	na	50	Cc–Dol	na	Aar Massif: Upper Jurassic (carbonate dominated)	Doldenhorn nappe	Herwegh Pfiffner (2005)	BB'
UR-17-01-A	2655833	1167115	2700	310	10	14	40	RSCM	Luensdorf (2017) poly3	Aar Massif: Middle Jurassic (clay dominated)	Dossenhuette, Dossenkeil	Nibourel et al. (2021)	CC'
UR-17-01-B	2655833	1167115	2695	303	14	6	40	RSCM	Luensdorf (2017) poly3	Aar Massif: Upper Jurassic (carbonate dominated)	Dossenhuette, Dossenkeil	Nibourel et al. (2021)	CC'
UR-17-01-C	2655833	1167115	2690	314	15	11	40	RSCM	Luensdorf (2017) poly3	Aar Massif: Upper Jurassic (carbonate dominated)	Dossenhuette, Dossenkeil	Nibourel et al. (2021)	CC'
m-pc-wendenjo(	2676990	1180400	2640	295	4	4	40	RSCM	Luensdorf (2017) poly3	Aar Massif: Variscan sedimentary rocks	Wendenjoch	Nibourel et al. (2018)	DD'
m-pc-wendenjo(	2676990	1180400	2640	288	18	36	40	RSCM	Luensdorf (2017) poly3	Aar Massif: Variscan sedimentary rocks	Wendenjoch	Nibourel et al. (2018)	DD'
FA-15-05	2679145	1175977	2540	345	24	24	40	RSCM	Luensdorf (2017) poly3	Aar Massif: Tertiary sediments	Chli Griessenhorn	Nibourel et al. (2018)	DD'
FA-15-13	2677181	1174049	2750	377	9	5	40	RSCM	Luensdorf (2017) poly3	Aar Massif: Variscan sedimentary rocks	Chalchtalluecke	Nibourel et al. (2018)	DD'
RU-15-02	2711270	1185807	2850	324	7	17	40	RSCM	Luensdorf (2017) poly3	Aar Massif: Variscan sedimentary rocks	Val Russein, Sandpass	Nibourel et al. (2021)	DD'
RU-15-03	2711369	1185829	2900	320	11	14	40	RSCM	Luensdorf (2017) poly3	Aar Massif: Middle Jurassic (clay dominated)	Val Russein, Sandpass	Nibourel et al. (2021)	DD'
WE-16-03	2673762	1179258	1970	283	10	22	40	RSCM	Luensdorf (2017) poly3	Aar Massif: Middle Jurassic (clay dominated)	Wendental	Nibourel et al. (2021)	DD'
FA-16-02	2678282	1174866	2210	345	25	28	40	RSCM	Luensdorf (2017) poly3	Aar Massif: Middle Jurassic (clay dominated)	Faernigen	Nibourel et al. (2021)	DD'
WE-16-02-2	2676803	1180346	2609	267	13	20	40	RSCM	Luensdorf (2017) poly3	Aar Massif: Triassic (clay dominated)	Wendensattel	Nibourel et al. (2018)	DD'
UG13_6	2679006	1160590	2100	489	na	na	50	RSCM	Beyssac et al. (2002)	Urseren-Garvera Zone	urseren-garvera	Erne (2014)	DD'
UG13_8	2681696	1161833	1670	515	na	na	50	RSCM	Beyssac et al. (2002)	Urseren-Garvera Zone	urseren-garvera	Erne (2014)	DD'
m-pc-windgaelle	2699080	1183780	2440	316	5	12	40	RSCM	Luensdorf (2017) poly3	Aar Massif: Tertiary sediments	Unteres Furkli, ob. Erzgruben	Nibourel et al. (2021)	EE'
MA-15-01	2704158	1183930	1500	325	16	20	40	RSCM	Luensdorf (2017) poly3	Aar Massif: Middle Jurassic (clay dominated)	Griess	Nibourel et al. (2021)	EE'
KL-15-06	2698115	1191772	850	272	11	26	40	RSCM	Luensdorf (2017) poly3	North-Helvetic Flysch	Sulztal	Nibourel et al. (2021)	EE'
WI-16-15	2701976	1185200	3137	315	9	20	40	RSCM	Luensdorf (2017) poly3	Aar Massif: Upper Jurassic (carbonate dominated)	Ruchen	Nibourel et al. (2021)	EE'
WI-16-16	2703169	1186211	2611	286	14	16	40	RSCM	Luensdorf (2017) poly3	Aar Massif: Tertiary sediments	Ruchen	Nibourel et al. (2021)	EE'
SI-17-02	2695596	1183861	1550	290	17	13	40	RSCM	Luensdorf (2017) poly3	Aar Massif: Upper Jurassic (carbonate dominated)	Kilcherberg (Silenen)	Nibourel et al. (2021)	EE'
SI-17-03	2696118	1184375	2060	292	6	13	40	RSCM	Luensdorf (2017) poly3	North-Helvetic Flysch	Riedersegg (Silenen)	Nibourel et al. (2021)	EE'
SI-17-04	2696751	1184070	2280	305	14	16	40	RSCM	Luensdorf (2017) poly3	North-Helvetic Flysch	Riedersegg (Silenen)	Nibourel et al. (2021)	EE'
SI-17-05	2694873	1186124	1520	293	8	15	40	RSCM	Luensdorf (2017) poly3	Aar Massif: Middle Jurassic (clay dominated)	Efeli (Silenen)	Nibourel et al. (2021)	EE'
2	2704050	1169000	1580	432	6	na	50	RSCM	Beyssac et al. (2002)	Penninic or Austroalpine	MF	Wiederkehr et al. (2011)	EE'
3	2709040	1170050	1420	392	5	na	50	RSCM	Beyssac et al. (2002)	Penninic or Austroalpine	MF	Wiederkehr et al. (2011)	EE'
FR-15-02	2723953	1181940	1320	359	15	9	40	RSCM	Luensdorf (2017) poly3	Aar Massif: Middle Jurassic (clay dominated)	Val Frisal	Nibourel et al. (2021)	FF'
DA-17-01	2719726	1183094	2772	344	18	13	40	RSCM	Luensdorf (2017) poly3	Aar Massif: Upper Jurassic (carbonate dominated)	Piz Dadens	Nibourel et al. (2021)	FF'
DA-17-02	2718224	1183230	2640	345	19	7	40	RSCM	Luensdorf (2017) poly3	Aar Massif: Middle Jurassic (clay dominated)	Val Frisal (N Brigelserhoerner)	Nibourel et al. (2021)	FF'
IN22	2665047	1173280	1520	306	13	15	40	RSCM	Luensdorf (2017) poly3	Aar Massif: Middle Jurassic (carbonate dominated)	Pfaffenkopf	Nibourel et al. (2021)	FF'
BL03	2665249	1171415	2222	385	69	30	40	RSCM	Luensdorf (2017) poly3	Aar Massif: Variscan sedimentary rocks	Baenzlaui	Nibourel et al. (2021)	FF'
Gl 07-08	2719820	1198112	758	260	na	na	25	RSCM	Lahfid et al. (2010)	North-Helvetic Flysch	Glarnerland/Sernf	Lahfid et al. (2010)	FF'
Gl 07-09	2718877	1194958	1033	300	na	na	25	RSCM	Lahfid et al. (2010)	North-Helvetic Flysch	Glarnerland/Sernf	Lahfid et al. (2010)	FF'
Gl 07-10	2717848	1191868	1111	310	na	na	25	RSCM	Lahfid et al. (2010)	North-Helvetic Flysch	Glarnerland/Sernf	Lahfid et al. (2010)	FF'
Gl 07-11	2717545	1192574	809	310	na	na	25	RSCM	Lahfid et al. (2010)	North-Helvetic Flysch	Glarnerland/Sernf	Lahfid et al. (2010)	FF'

Table S2: Table containing the compilation of the peak temperature data (°C) used in this study. Coordinate system: CH1903+ /LV95.

REFERENCES

Baumberger, R., 2015. Quantification of Lineaments: Link between Internal 3D Structure and Surface Evolution of the Hasli Valley (Aar Massif, Central Alps, Switzerland). PhD Thesis. Bern University, pp. 132.

Baumberger, R., Herwegh, M., Kissling, E., 2022. Remote sensing and field data based structural 3D modelling (Haslital, Switzerland) in combination with uncertainty estimation and verification by underground data. 3D Digital Geological Models: From Terrestrial Outcrops to Planetary Surfaces, 159-197.

Berger, A., Mercolli, I., Herwegh, M., and Gnos E.: Geological Map of the Aar Massif, Tavetsch and Gotthard Nappes 1: 100 000, Federal Office of Topography Swisstopo, Wabern, 2017

Bond, C.E., Philo, C., Shipton, Z.K., 2011. When there isn't a Right Answer: interpretation and reasoning, key skills for twenty-first century geoscience. Int. J. Sci. Educ. 33, 629–652. https://doi.org/10.1080/09500691003660364.

Brisson, S., Wellmann, F., Chudalla, N., von Harten, J., & von Hagke, C. (2023). Estimating uncertainties in 3-D models of complex fold-and-thrust belts: A case study of the Eastern Alps triangle zone. Applied Computing and Geosciences, 18, 100115.

Caumon, G., Lepage, F., Sword, C. H., Mallet, J. L., 2004. Building and editing a sealed geological model. Mathematical Geology, 36(4), 405-424.

Collet, L. and Paréjas, E.: Carte géologique de la chaîne de la Jungfrau, 1:25 000, Francke, Bern, 1928.

Diehl, T., Kissling, E., Herwegh, M., & Schmid, S. M., 2021. Improving Absolute Hypocenter Accuracy With 3D Pg and Sg Body-Wave Inversion Procedures and Application to Earthquakes in the Central Alps Region. Journal of Geophysical Research: Solid Earth, 126(12), e2021JB022155.

Hänni, R., Pfiffner, O. A., 2001. Evolution and internal structure of the Helvetic nappes in the Bernese Oberland. Eclogae Geologicae Helvetiae, 94(2), 161- 171.

Herwegh, M., Pfiffner, O.-A., 2005. Tectono-metamorphic evolution of a nappe stack: A case study of the Swiss Alps. Tectonophysics 404 (1-2), 55–76.

Herwegh, M., Berger, A., Baumberger, R., Wehrens, P., Kissling, E., 2017. Large-scale crustal-block-extrusion during late Alpine collision. Sci. Rep. 7 (1), 1–10.

Herwegh, M., Berger, A., Glotzbach, C., Wangenheim, C., Mock, S., Wehrens, P., Baumberger, R., Egli, D., Kissling, E., 2020. Late stages of continent-continent collision: timing, kinematic evolution, and exhumation of the Northern rim (Aar Massif) of the Alps. Earth Sci. Rev. 200, 102959 https://doi.org/10.1016/j.earscirev.2019.102959.

Krayenbuhl, T. and Steck, A.: Structure and kinematics of the Jungfrau syncline, Faflertal (Valais, Alps), and its regional significance, Swiss Journal of Geosciences, 102, 441–456, https://doi.org/10.1007/s00015- 009-1333-1, 2009.

Krebs, J.: Geologische Beschreibung der BlümlisalpGruppe, Beiträge zur Geol. Karte der Schweiz, N.F. 54, Francke, Bern, 1925.

Mair, D., Lechmann, A., Herwegh, M., Nibourel, L., Schlunegger, F., 2018. Linking Alpine deformation in the Aar Massif basement and its cover units–the case of the Jungfrau–Eiger Mountains (Central Alps, Switzerland). Solid Earth 9, 1099–1122.

Musso Piantelli, F., Mair, D., Berger, A., Schlunegger, F., Wiederkehr, M., Kurmann, E., Moeri, A., Baumberger, R., and Herwegh, M. (2022). 4D reconstruction of the Doldenhorn nappe-basement system in the Aar massif: Insights into late-stage continent-continent collision in the Swiss Alps. Tectonophysics, 843, 229586.

Musso Piantelli, F., Truttmann, S., & Herwegh, M. (2023). The control of collisional tectonics over valley morphology: the case of the largest glacier in the European Alps. Terra Nova.

Musso Piantelli, F., 2023. 4D reconstruction of the Aar Massif: An evolutionary history from a passive margin to the Central Swiss Alpine valleys. (PhD Thesis). Universität Bern, Bern. https://boristheses.unibe.ch/id/eprint/5475

Nibourel, L., Berger, A., Egli, D., Heuberger, S., & Herwegh, M. (2021). Structural and thermal evolution of the eastern Aar Massif: insights from structural field work and Raman thermometry. Swiss journal of geosciences, 114(1), 9.

Nibourel, L., 2019. The structural and thermo-kinematic evolution of the eastern Aar Massif, Switzerland. Institut für Geologie, University of Bern, pp. 1–175 PhD thesis.

Pakyuz-Charrier, E., Lindsay, M., Ogarko, V., Giraud, J., Jessell, M., 2018. Monte Carlo simulation for uncertainty estimation on structural data in implicit 3-D geological modeling, a guide for disturbance distribution selection and parameterization. Solid Earth 9, 385–402. https://doi.org/10.5194/se-9-385-2018.

Pfiffner, O. A., Lehner, P., Heitzmann, P., Mueller, S., & Steck, A. (1997). Deep structure of the Swiss Alps: results of NRP 20. Birkhäuser.

Pfiffner, O. A., Ramsay, J. G., & Schmid, S. M. (2011). Structural map of the Helvetic Zone of the Swiss Alps. Geological special map, 1(100,000).

Schneeberger, R., de La Varga, M., Egli, D., Berger, A., Kober, F., Wellmann, F., Herwegh, M., 2017. Methods and uncertainty estimations of 3-D structural modelling in crystalline rocks: a case study. Solid Earth 8, 987-1002.

Sibson, R. H., 1977. Fault rocks and fault mechanisms. Journal of the Geological Society, 133(3), 191–213.

Wehrens, P.C., 2015. Structural Evolution in the Aar Massif (Haslital Transect): Implications for Mid-Crustal Deformation. Institut für Geologie, University of Bern, pp. 1–139 PhD thesis.

Wehrens, P., Berger, A., Peters, M., Spillmann, T., Herwegh, M., 2016. Deformation at the frictional-viscous transition: evidence for cycles of fluid-assisted embrittlement and ductile deformation in the granitoid crust. Tectonophysics 693, 66–84.

Wehrens, P., Baumberger, R., Berger, A., Herwegh, M., 2017. How is strain localized in a meta-granitoid, mid-crustal basement section? Spatial distribution of deformation in the central Aar massif (Switzerland). J. Struct. Geol. 94, 47–67.

Wellmann, J.F., Horowitz, F.G., Schill, E., Regenauer-Lieb, K., 2010. Towards incorporating uncertainty of structural data in 3D geological inversion. Tectonophysics 490, 141–151. https://doi.org/10.1016/j.tecto.2010.04.022.

Wellmann, J.F., Regenauer-Lieb, K., 2012. Uncertainties have a meaning: information entropy as a quality measure for 3-D geological models. Tectonophysics 526, 207–216. https://doi.org/10.1016/j.tecto.2011.05.001.

Wellmann, J.F., Lindsay, M., Poh, J., Jessell, M., 2014. Validating 3-D structural models with geological knowledge for improved uncertainty evaluations. Energy Proc. 59, 374–381. https://doi.org/10.1016/j.egypro.2014.10.391.

Wellmann, F., Caumon, G., 2018. 3D structural geological models: concepts, methods, and uncertainties. In: Advances in Geophysics, vol. 59. Elsevier, pp. 1–121. https:// doi.org/10.1016/bs.agph.2018.09.001.